ORIGINAL ARTICLE

CrossMark

4D wet refractivity estimation in the atmosphere using GNSS tomography initialized by radiosonde and AIRS measurements: results from a 1-week intensive campaign

Pedro Benevides[1] · Joao Catalao[1] · Giovanni Nico[2] · Pedro M. A. Miranda[1]

© Springer-Verlag GmbH Germany, part of Springer Nature 2018

Abstract

A Global Navigational Satellite System (GNSS) tomography system is implemented in the Lisbon area, Portugal, to estimate the water vapor dynamics at a local scale. A field experiment was carried out, in which a series of temporary GNSS stations were installed, increasing the network from 9 permanent stations to a total of 17 GNSS stations. A radiosonde campaign was also performed with high sampling launches, at 4-h intervals, for 1 week. A time series of hourly 3D wet refractivity solutions were obtained during the radiosonde campaign. Radiosonde and Atmospheric Infrared Sounder (AIRS) measurements were used to compute wet refractivity profiles to initialize and update the tomography solutions. The dependence of the GNSS tomography solution on the initial conditions obtained from both radiosonde and AIRS measurements, and their updating frequencies are studied. It is found that the GNSS tomography continuous measurement of the atmospheric refractivity provides solutions with an RMS mean of about 2 g/m^3.

Keywords Global Positional System (GPS) · Global Navigational Satellite System (GNSS) · Atmospheric modeling · Tomography · Precipitable water vapor (PWV) · Atmospheric infrared sounder (AIRS)

Introduction

The GNSS technique has proved its capacity for sensing the spatial and temporal variations of the tropospheric water vapor with an accuracy comparable to direct meteorological observations (Guerova et al. 2016; Lu et al. 2016). GNSS tomography applications have taken integrated water vapor (IWV) measurements one step further, providing tridimensional maps of the troposphere (Flores et al. 2000; Aghajany and Amerian 2017). This became possible due to the worldwide increase of GNSS permanent stations and the development of new GNSS systems such as Galileo and BeiDou (Bender et al. 2011). The tomographic model requires a dense network of GNSS stations with a homogeneous spatial distribution (Brenot et al. 2014). The network configuration constrains the horizontal resolution of the discrete tomographic grid used to divide the troposphere, which is also vertically discretized, i.e., a voxel. The water vapor is estimated by properly combining all Slant Wet Delay (SWD) observations passing through each voxel (Flores et al. 2000). The SWD is the result of the wet refractivity variation along the satellite line-of-sight and is proportional to the water vapor content (Bevis et al. 1992). The estimation of the wet refractivity is obtained solving a system of equations with SWD observations measured by the GNSS stations during a short period of time (Champollion et al. 2005).

Due to the GNSS acquisition geometry, with the line-of-sights falling within an inverted cone (Benevides et al. 2015a), a large number of voxels are not intersected by any observation, especially for SWD closer to the horizon, having low elevation angles (Rohm 2013). Taking care of system underdetermination requires additional physical constraints

✉ Pedro Benevides
  pjbenevides@fc.ul.pt

  Joao Catalao
  jcfernandes@fc.ul.pt

  Giovanni Nico
  g.nico@ba.iac.cnr.it

  Pedro M. A. Miranda
  pmmiranda@fc.ul.pt

[1] Instituto Dom Luiz, Faculdade de Ciências, University of Lisbon, 1749-016 Lisbon, Portugal

[2] Instituto per le Applicazioni del Calcolo, ConsiglioNazionale delle Ricerche, 70126 Bari, Italy

about the wet refractivity spatial variation (Bender et al. 2011). There are several approaches to solve this ill-conditioned problem: add some constraints using a priori information, i.e., wet refractivity profiles from meteorological data (Champollion et al. 2005), or add some spatial constraints to smooth the wet refractivity field (Flores et al. 2000). Both approaches can be implemented using the Bayesian approach (Menke 2012). With the increasing number of GNSS stations and future GNSS systems, it is expected that the number of SWD observations per unit of time will increase and the geometric dilution of precision (GDOP) index will decrease, due to the different mission's geometry. Consequently, the number of empty voxels is reduced, minimizing the ill-conditioned problem and improving the GNSS tomographic solution (Benevides et al. 2017). However, the GNSS tomography will still have a limited ability to resolve the vertical structure of the atmosphere, particularly above the highest station. This is important as water vapor concentrates in the lower layers of the troposphere. As a consequence, the state of the atmosphere at a given instant should be introduced as an initial condition of the model. A good strategy is to initiate the tomography with a wet refractivity vertical profile, which can be obtained from a standard atmospheric model or from meteorological data (Zhang et al. 2015). Radiosondes are still the most used and more reliable data to measure the local water vapor content (Mateus et al. 2015).

Remote sensing data from specific sensors can also be useful to derive the tropospheric water vapor properties (Benevides et al. 2015b, 2016). The Atmospheric Infrared Sounder (AIRS) mission, composed by a hyperspectral sensor that observes infrared and microwave radiation from earth, provides a rapid and global coverage over land mass and ocean, where atmospheric observations are very scarce. AIRS wet refractivity profiles have a worldwide high spatial sampling rate, which is an advantage over the radiosonde method. The major drawback of AIRS is that the regular presence of clouds in the troposphere implies a significant limitation in the vertical resolution measurements when compared with the high sampling provided by a radiosonde (Olsen et al. 2013).

In this work, we investigate the impact of increasing the updating frequency of the initial condition on the GNSS tomography solution. The main motivation is to understand if regional GNSS networks can provide accurate 3D wet refractivity estimates without ancillary data and define the maximum time interval to reset the system with an updated state of wet refractivity. The impact of the initial wet refractivity state introduced in the model is evaluated along a time series of sequential tomographic reconstructions of wet refractivity maps. With this objective, a field experiment was carried out in the Lisbon area, Portugal, where 8 GNSS stations were temporarily installed resulting in a densified network of 17 receivers (1 station/16.5 km^2). The experiment

took place during 3 weeks of July 2013, in coordination with a radiosonde campaign where high sampling launches within a 4-h interval were performed for about 1 week. Radiosonde wet refractivity profiles were used to initiate and update a temporal sequence of tomographic solutions, during the radiosonde week campaign. Another independent tomography series was generated using wet refractivity profiles derived from AIRS instead. An additional tomography temporal sequence was processed using only one radiosonde profile initiation, with no update, to analyze the temporal evolution of the refractivity estimation error. In the end, both radiosonde profiles and AIRS acquisitions are combined into a tomography solution. The results are discussed in terms of accuracy assessed by comparing with wet refractivity estimated from data acquired by the radiosondes not used for the initialization of the tomography.

GNSS tomography

Water vapor measurements with GNSS are based on the refractivity differences in the propagation medium, mainly related to the water vapor variations in the troposphere. The atmospheric refractivity can be decomposed into two components: hydrostatic and wet. The former, essentially caused by atmospheric dry gases, varies smoothly in time and can be estimated accurately from surface pressure values (Tregoning and Herring 2006). The latter, which is caused by the water vapor content, can be estimated from GNSS as (Flores et al. 2000):

$$\text{SWD} = 10^{-6} \int N_w \times ds = \text{ZWD} \times \text{mf}_w(\varepsilon)$$
$$+ \left(G_{NS} \times \cos(\alpha) + G_{EW} \times \sin(\alpha) \right) \times \text{mf}_g(\varepsilon, \alpha),$$

$$(1)$$

where N_w is the wet refractivity, ZWD is the Zenith Wet Delay, mf_w is a wet mapping function that is a function of the satellite elevation angle ε, mf_g is a horizontal gradient function that is dependent on the satellite azimuth direction a and also dependent on ε, G_{NS} is the north–south wet gradient component, and G_{EW} the wet gradient component relative to the east–west direction. ZWD is the difference between the zenith total delay (ZTD), estimated in the GNSS processing, and the zenith hydrostatic delay (ZHD) estimated from the surface pressure measurements. The SWD is nearly proportional to the precipitable water vapor (PWV) with a conversion factor that depends on the mean temperature of the atmosphere (Bevis et al. 1992).

The 3D wet refractivity is estimated by discretizing the atmosphere, defining a three-dimensional grid of voxels over a GNSS network. The SWD observations from each GNSS station are ray traced into the tomographic grid space, providing the distance traveled by the GNSS signal

in each voxel. Here, we have used the simplest discretization approach based on a constant refractivity within a voxel (Champollion et al. 2005). One parameter per voxel must be estimated. The unknown wet refractivity (N_w) are related to the observations (SWD) by the following system of equations:

$$\mathrm{SWD} = A\, N_w \equiv \begin{bmatrix} \mathrm{SWD}_1 \\ \vdots \\ \mathrm{SWD}_n \end{bmatrix} = \begin{bmatrix} d_{11} & \dots & d_{1m} \\ \vdots & \ddots & \vdots \\ d_{n1} & \dots & d_{nm} \end{bmatrix} \begin{bmatrix} N_{w1} \\ \vdots \\ N_{wm} \end{bmatrix}, \quad (2)$$

where SWD represents the vector of observations, N_w represents the vector of the wet refractivity unknowns, and A is a matrix that sets the tomographic grid configuration. The A matrix includes the subpath distances d_{nm}, for each observation traveled through the respective voxels (Flores et al. 2000). With the assumption of a Gauss distribution for the a priori and measurement errors, the ill-conditioned nature of the problem can be addressed by utilizing discrete inverse theory. The 3D refractivity field N_w can be reconstructed from an a priori refractivity field using a Bayesian approach (Champollion et al. 2005):

$$N_w = N_0 + K\ \left(\mathrm{SWD} - AN_0\right) \quad K = \left(A^T C^{-1} A + C_0^{-1}\right)\left(A^T C^{-1}\right), \tag{3}$$

where N_0 represents a wet refractivity initial solution for the tomographic grid, C is a diagonal matrix of the observation variances, C_0 the covariance matrix of the initial solution, and K the Kalman gain matrix. The covariance matrix is implemented following the work of Champollion et al. (2005), adapted to this data in Benevides et al. (2016). The initial solution in (3) can be estimated from several types of data, such as radiosondes and other meteorological data (Champollion et al. 2009), data from numerical weather models (NWM) (Labbouz et al. 2013) and standard atmospheric models (Perler et al. 2011), and even from remote sensing data (Benevides et al. 2015b).

The distinctness in the GNSS tomography technique, which sets it apart from most tomography models, is that the observations are controlled by the transmitter–receiver geometry given the variable satellite orbital dynamics in space and the fixed GNSS positions on the ground. This results in several voxels not crossed by any observation. The proportion of those voxels depends on the spatial density of the GNSS stations versus the tomographic grid horizontal resolution. It is important to notice that the tomography problem is itself ill-posed, even without empty voxels, but the degree of ill-posedness increases with empty cells (Bender et al. 2011). Usually, numerical constraints are introduced in the GNSS tomography system of equations. However, in the case of a low percentage of empty voxels, provided for example from a dense GNSS network, the constraints can be softened to obtain a more realistic solution of the tropospheric wet refractivity (Rohm 2013).

Experiment setup

The SMOG (structure of moist convection in high-resolution GNSS observations and models) project campaign took place from July 17–23, 2013, corresponding to DOY (day of year) 198 to 204, in the area of Lisbon, Portugal. In general, the GNSS network should be able to see relevant features in synoptic weather systems, helping us to understand the dynamics of severe storms, such as those occurring in recent years, where available images and radar clearly show very heterogeneous atmospheric water fields, such as dry intrusions. Because of its short duration, the campaign was, however, designed to look at recurrent features of the low-level summer circulation, namely those associated with the diurnal cycle of the sea breeze, which is also thought to have a large impact in the vertical distribution of water vapor (Miranda et al. 2013).

In the area of Lisbon, there are nine permanent GNSS stations belonging to the ReNEP and SERVIR networks, operated by the National Mapping Agency (Direção-Geral do Território) and Geospatial Information Center (Portuguese Army). During the campaign period, the existing GNSS network was complemented with eight more GNSS receivers. The merged network had 17 GNSS receivers within a square area of about 60×60 km². The location of the temporary GNSS stations was chosen to minimize the number of empty voxels and improve the vertical discretization. Other important location constraints are related to installation feasibility, like the need to be a fenced or guarded place, have electrical power and allow to install the GNSS antenna without significant horizon obstructions. The area covered by the network is characterized by complex topography with moderate elevation on the west ($H \approx 200$ m) and flat topography with low elevation on the east, around the Tagus estuary. The highest stations are SMG3 on the top of Sintra's palace ($H \approx 500$ m) and ARRA on Arrábida sierra ($H \approx 400$ m). The tomographic grid was divided into five voxels in the longitudinal direction and six voxels in the latitudinal direction, corresponding to a horizontal voxel size of about 11×11 km². All these features can be seen in Fig. 1. The grid limits were set to have most of the stations located close to the boundary of the voxels, minimizing the number of empty voxels. The vertical grid resolution was composed of 18 layers, with variable spacing, defined between the limits of the terrain surface and the ellipsoidal surface at the height of 10 km. This top boundary should be close enough to the local tropopause to ensure that the water vapor content at this height is null in most weather conditions (Benevides et al. 2016). The vertical spacing starts at
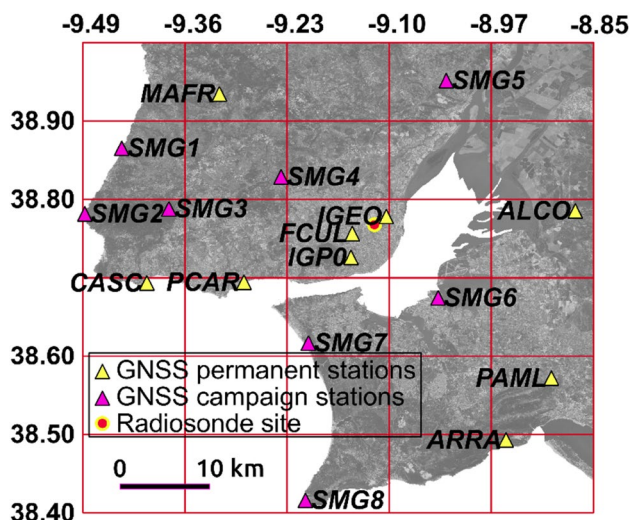
Fig. 1 Study area of Lisbon with the tomography grid overlaid. The background is based on Sentinel-2 data

500 m, following an increasing layer spacing with height, to allow a close approximation to the typical water vapor decay with altitude (Benevides et al. 2017). The GNSS temporary network was implemented in July 2013, overlapping the SMOG radiosonde launching campaign. The radiosondes were launched every 4 h at the Lisbon airport meteorological station, which also corresponds to the tomographic grid center location (Fig. 1). The AIRS wet refractivity profiles were also selected during the radiosonde campaign and have a rate of two acquisitions per day.

GNSS atmospheric processing

The site coordinates and ZTD time series were determined using the GPS data processing software GAMIT/GLOBK, using double-difference processing strategies. The processing scheme is divided into two steps: (a) using GAMIT/GLOBK to determine the best coordinates for the GNSS network and (b) using tight constraints on the site coordinates to estimate enhanced tropospheric parameters. The ionospheric-free linear combination is used (Herring et al. 2010). The stations are constrained to the ITRF08 reference frame using 58 worldwide International GNSS Service (IGS) stations. IGS precise final orbits are also used. This provides better coordinates estimate and reduces the correlation between tropospheric parameters of different stations. To remove the edge effect at the start and end of daily ZTD solutions, a time overlap window strategy was adopted in (b) (Benevides et al. 2015a). This strategy is configured by four processing sessions with 12-h duration (21:00–09:00, 03:00–15:00, 09:00–21:00, 15:00–03:00 UTC), combining the central 6 h of each process into a 24-h daily record of estimated tropospheric data. Orbits adjusted from (a) are

also used to avoid coarse orbit estimate usually obtained with only 12-h processing. The ZTD is determined from a stochastic function variation of the ZHD using piecewise linear interpolation between time steps, constrained to a Gauss–Markov process with a power density function of 1 cm/h$^{1/2}$ for the atmospheric zenith parameters and 2 cm/h$^{1/2}$ for the gradient parameters. Pressure and climate data from the European Center for Medium-Range Weather Forecasting reanalysis (ECMWF) are used to estimate ZHD every 6 h. A cutoff angle of 5° is used together with the Vienna Mapping Function model (VMF) to estimate the ZWD (Boehm et al. 2006). An ocean loading model derived from tides, and an atmospheric pressure loading model is also used (Herring et al. 2010). The atmospheric parameters are estimated with a time sampling of 15 min, together with the horizontal variation gradients with a 30-min interval. This provides an adequate time sampling to implement the GNSS tomography technique, still not increasing too much the GPS processing time (Champollion et al. 2005).

The SWD observations are reconstructed from (1) applying the aforementioned VMF, considering the mf$_w$ coefficient (depending on DOY, the station latitude and height) and observing for each GNSS station the satellite elevation angles at each instant. Several authors, such as Champollion (2004) and Nilsson et al. (2007), have verified that the accuracy of the tropospheric gradients is imprecise compared to the ZWD, and because of that, we decided not to include the wet gradients. The result is the slant integrated observation of the wet refractivity content, SWD or Slant Water Vapor (SWV) (Champollion et al. 2005). In this work, we have chosen to use the SWV definition because it provides more meaningful values for meteorological data comparison. Given the 30-s data sampling of the GNSS network in the study area, we can generate a high number of SWV observations for each GNSS receiver to use in the tomography model. This helps to have a more robust tomographic solution. However, we cannot ray trace SWV in arbitrary direction as this would introduce artifacts in the refractivity reconstruction. To model the increasing error of the GNSS slant observations with decreasing elevation angle (Boehm et al. 2006), we adopt the elevation error model implemented in GAMIT (Herring et al. 2010). The observation error σ_{swv} is determined to combine the ZWD error σ_{zwd} obtained from GAMIT with the modeled elevation error σ_ε, setting the observation variances in C matrix (Eq. 3) (Benevides et al. 2016). The diagonal elements of the C matrix are given by (Herring et al. 2010):

$$\sigma_{\mathrm{SWV}}^2 = \sigma_{\mathrm{ZWD}}^2 k_{\mathrm{ZWD}} + \sigma_\varepsilon^2 k_\varepsilon \qquad \sigma_\varepsilon = \left(a^2 + \frac{b^2}{\sin \varepsilon} \right), \qquad (4)$$

where k_{zwd} and k_ε are empirical constants, set in this work to 1, and a is equal to 4.3 mm and b is equal to 7.0 mm. For

simplicity, we assume that the covariances in matrix C are zero.

Following the observations determination, it is important to define a time interval to allow the GPS ray paths to fill in the voxels of the tomographic grid. The interval should be large enough to gather a significant number of observations, maximizing the number of crossed voxels, and tight enough to not mitigate important water vapor features (Champollion et al. 2005). Therefore, a 30 min interval was chosen to generate 3D tomography solutions.

Atmospheric infrared sounder and radiosonde data retrieval

The AIRS sensor on board of NASA's Aqua satellite, with a polar sun-synchronous orbit, is a hyperspectral infrared instrument with 2378 channels, with two multichannel microwave instruments. It was designed to observe globally the vertical structure of an atmospheric column, measuring several geophysical variables including water vapor (Olsen et al. 2013). We have chosen version 6 level-2 products, with cloud calibrated radiances and geolocated values. There are generally 240 granules acquisitions worldwide per day, with a repeating cycle of about two measurements at approximated locations within a few km. Each granule corresponds to 6 min of instrument scanning, covering approximately 1650×2250 km^2 of terrain area, cross-track per along-track, and is composed by 30 cross-track per 45 along-track profile measurements, corresponding to a total of 1350 retrievals in one granule. The granule grid spacing has a fixed distance of about 55 km along-track and an uneven cross-track spacing; 40 to about 100 km. However, the nominal spatial resolution for each profile is estimated to be about 13.5 km (Divakarla et al. 2006). Nevertheless, for each granule, the scanned profiles will fall in different locations within the tomographic grid area. Thus, we only select the profile with the smaller distance to the radiosonde station location, due to its central position relative to the tomographic grid. The level-2 products have 28 height levels, with some geophysical variables only registered at half of them. Instead of using directly the water vapor variables from these products, we have chosen to calculate the wet refractivity of the AIRS profiles.

The quantities measured in the AIRS profiles, and also by radiosonde launches, are converted into wet refractivity values using temperature, relative humidity and pressure measurements at each altitude level, following the expressions:

$$N_w = Z_w^{-1}\left(k_2\frac{e}{T} + k_3\frac{e}{T^2}\right), \tag{5}$$

$$e = \frac{6.112 r_h}{100}\exp\left(\frac{17.63\, t_c}{243.12 + t_c}\right), \tag{6}$$

where N_w is the wet refractivity, $k_2 = 71.6$ K/mbar and $k_3 = 3.75 \times 10^5$ K^2/mbar are water vapor empirical constants (Bevis et al. 1992), Z_w^{-1} is the empirical inverse wet compressibility, being very close to 1, e is the partial pressure of the water vapor in mbar, T is the temperature in Kelvin, t_c in the temperature in Celsius, and r_h is the relative humidity in percentage (Thayer 1974). The pressure values are used to derive the altitude using a hypsometric equation. The distinguishing factor here is given by the vertical sampling between the AIRS and radiosonde data. Radiosonde measurements are obtained with a time rate of 2 s, decimated by a factor of 10, preserving a high density of measurements along the tropospheric column. On the other hand, the AIRS profiles only have 14 values registered in the atmosphere, 8 of them below 10 km. However, for the sake of simplicity, linear interpolation for AIRS is performed to the tomographic grid vertical midpoints.

Results and discussion

To assess the impact of the initialization conditioning on the GNSS tomographic solution three groups of wet refractivity solutions were generated. Some details about the tomographic processing will be introduced first, which are common to all solution groups. To sequentially assimilate observations, we use an incremental approach, namely dead reckoning, with update step from time t_{n-1} to t_n given by [see (3)]:

$$N_w(t_n) = N_w(t_{n-1}) + K(t_n)\left[\text{SWD}(t_n) - A(t_n)N_w(t_{n-1})\right], \tag{7}$$

where $N_w(t_n)$ is the refractivity at time t_n, K is the weight matrix, A is the design matrix, and SWD are the observations. Typically, the incremental approach will drift over time as small errors accumulate and an updated state of the wet refractivity distribution in the atmosphere is needed to improve the accuracy of the wet refractivity predicted model. We investigate the question of how well tomographic solutions with different initializations approximate the radiosonde profiles measured with a 4-h sampling in 1 week. A time series of the 3D wet refractivity solution have been generated every hour. SWV observations, with a 30-s sampling, are obtained and grouped for a time period of 30 min, starting at the beginning of each hour. The geometrical constraint used in all tomography 30-min time steps is a horizontal inter-voxel smoothing based on the voxel distance (Rohm 2013). For the initialization time steps additional geometrical constraints are added; setting some top vertical layers with zero refractivity and setting the bottom vertical layer with refractivity values determined by a standard atmospheric profile (Benevides et al. 2017).

## Configuration of tomography solutions

The tomography solution groups can be characterized as follows. The time reference of these results is UTC, which in the region of Lisbon is less than 1 h from local solar time. Solution 1 is initialized with one radiosonde profile, 12:00 DOY 198, with continuously cycled solutions during the following 24 h except for the first day, 12:00 DOY 198 to 0:00 DOY 199, and initialized again each day at 0:00. Solution 2 is initialized with one AIRS profile (3:00 DOY 198) and re-initialized every time an AIRS profile is available over the study area, every day between 2:00–3:00 and 13:00–14:00, resulting in a continuous cycled solution of about 12 h except for the first day, 12:00 DOY 198 to 14:00 DOY 198. Solution 3 is obtained using again the first radiosonde profile for initialization, 12:00 DOY 198, but without any further re-initialization, resulting in a continuous solution of about 6 days. This third group is useful to assess the tomography reconstruction error evolution in time.

Vertical profile

The tomographic solutions were compared with radiosondes launched at the center of the tomographic grid. The launches took place every 4 h, starting 0:00 UTC, during 1 week. A visual comparison was made between the successive radiosonde profiles and the tomographic solutions. It is important to notice that the profiles extracted from the tomography are mean values of the refractivity within the voxel (11 km × 11 km × column height) over a period of 30 min. On the other hand, radiosonde measurements are two-dimensional and instantaneous. To compare the radiosonde measurement with the estimated voxel refractivity, the integrated value of the radiosonde along the height of each voxel was computed. Results considering solution 1 are presented in Fig. 2, showing the best and worst days, DOY 199 and 203, in terms of the root mean square (RMS) of the differences between tomography and radiosonde profiles. It is worth noting that the wet refractivity was converted to water vapor density (g/m^3) using in (1) the conversion factor proposed by Bevis et al. (1992). In this way we have that 1 kg/m^2 of IWV corresponds to 1 mm of PWV. Regarding this conversion factor, we have considered an estimated integrated mean temperature profile based on 3 years of radiosonde data in this study region (Mateus et al. 2014). As expected, at 0:00 the tomographic solution fits almost perfectly the radiosonde. Over time, the tomographic solution tends to deviate from the radiosonde, mostly at the lower troposphere. These

Fig. 2 Comparison of N_w vertical central profile, at DOY 199 (top) and DOY 203 (bottom), for tomography solution 1 (radiosonde initialization, red line and squares) and radiosonde measurements (blue line)
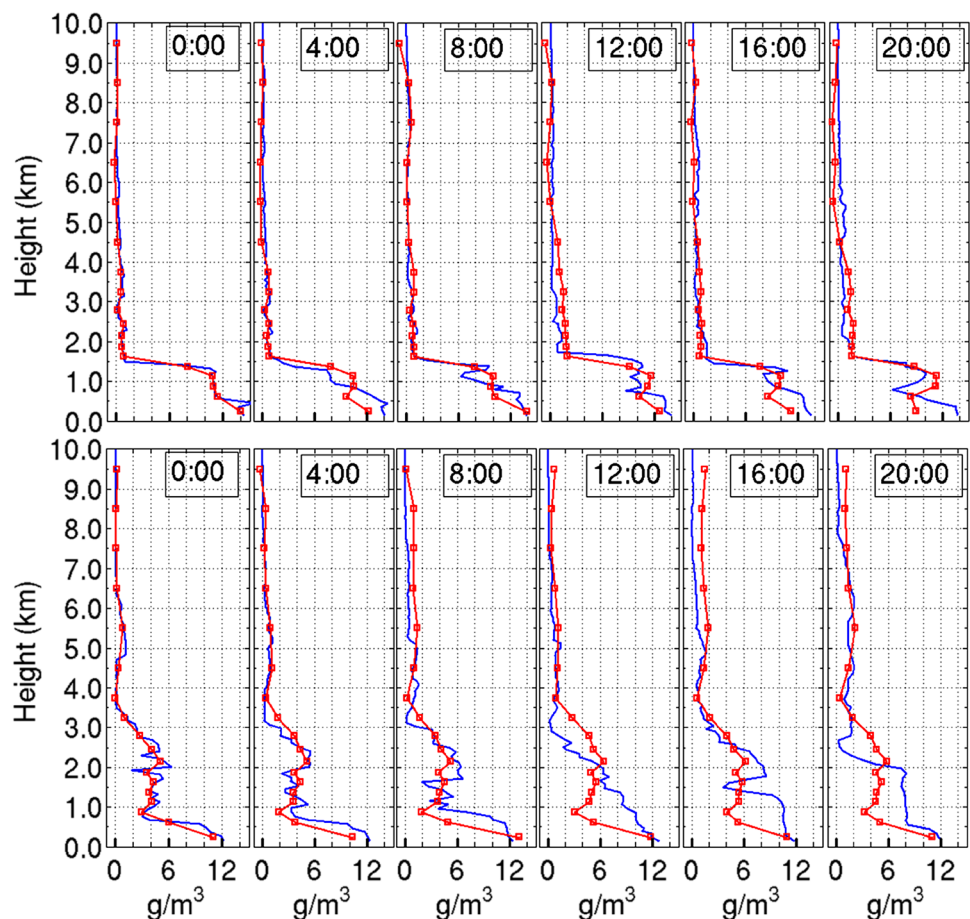
deviations have different signatures at each day. In DOY 199, the profile follows closely the radiosonde humidity variations until 20:00, and is even able to detect a dry intrusion near 1 km although it lacks resolution near the surface. In DOY 203 the radiosonde profile registers a transition from a very shallow humid boundary layer, below 800 m until 8:00, to a quasi-linear humidity profile at 12:00, which is cut in half by the establishment of the localized dry layer near 1500 m at 16:00. While the initial states, until 8:00 are very well captured by the tomography, the following evolution is not.

A similar comparison was also made between the successive radiosonde profiles and the tomographic solution initialized using the AIRS data (solution 2), which is presented in Fig. 3 jointly with the tomography solution initialized with radiosondes (solution 1). Here, we chose to display the midday (12:00) and the end of the day (20:00) for all the DOY in the campaign. Comparing, in general both tomography solutions, it clearly stands out that solution 2 has a smoother vertical profile, consistent with the coarser resolution of AIRS data. However, despite the fact that the tomography with AIRS is not able to represent the sharp humidity variations at the lower troposphere, most of these profiles are very close to the radiosonde in the lowest layer (0.5 km) and fit well again upwards of 3 km, and such fit remains throughout the day.
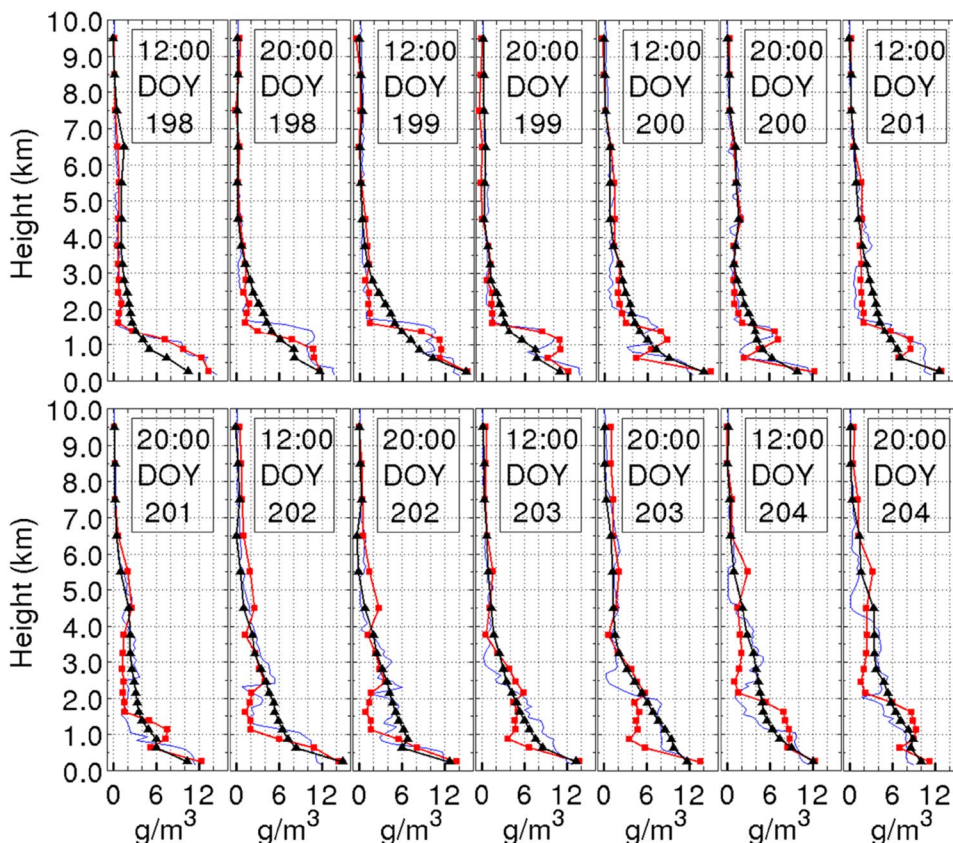
Figure 4 shows an error assessment of the two solutions, emphasizing their different vertical structure by aggregating the data in three separate layers: [0, 1.75] km, [2, 3.5] km, and [4, 10] km. In the bottom layer, solution 1 (radiosonde initialization) is on average more accurate. In the middle
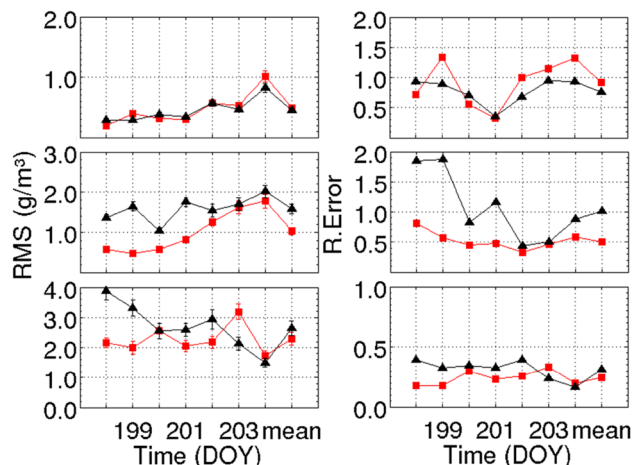

Fig. 4 Daily mean errors of the tomography solutions 1 (radiosonde initialization, red squares) and 2 (AIRS initialization, black triangles), against radiosonde launches in the three layers, from bottom to top: [0, 1.75] km, [2, 3.5] km, and [4, 10] km. Left column: RMS, right column: mean absolute relative error

Fig. 3 Comparison of water vapor profiles as obtained from radiosonde launches and tomography processing. Solutions at 12:00 and 20:00 UTC are displayed with N_w central profiles solutions for tomography solution 1 (radiosonde initialization; red line and squares) and tomography solution 2 (AIRS initialization; black line and triangles). The blue line represents the radiosonde data

layer, solution 1 is always more accurate, whereas in the top layer the AIRS solution is slightly better. In general, the AIRS solution is better at low levels in DOY 203 and 204, and is much worst in DOY 199 and 200 in the bottom and middle layers. The highest RMS values are, as expected, found in the wetter lower atmosphere, although the relative errors are smaller in that region.

Time evolution of tomographic solutions

The evolution of the different tomographic solutions is shown in Fig. 5, superimposed on the 4-h radiosonde profiles during the full field experiment. The radiosonde contour map indicates the strong variability of the local humidity profiles during the campaign, sometimes with very dry anomalies above 500 m, namely in DOY 200–201, 203, and 204, partially captured in solutions 1 and 2. The dry intrusion at
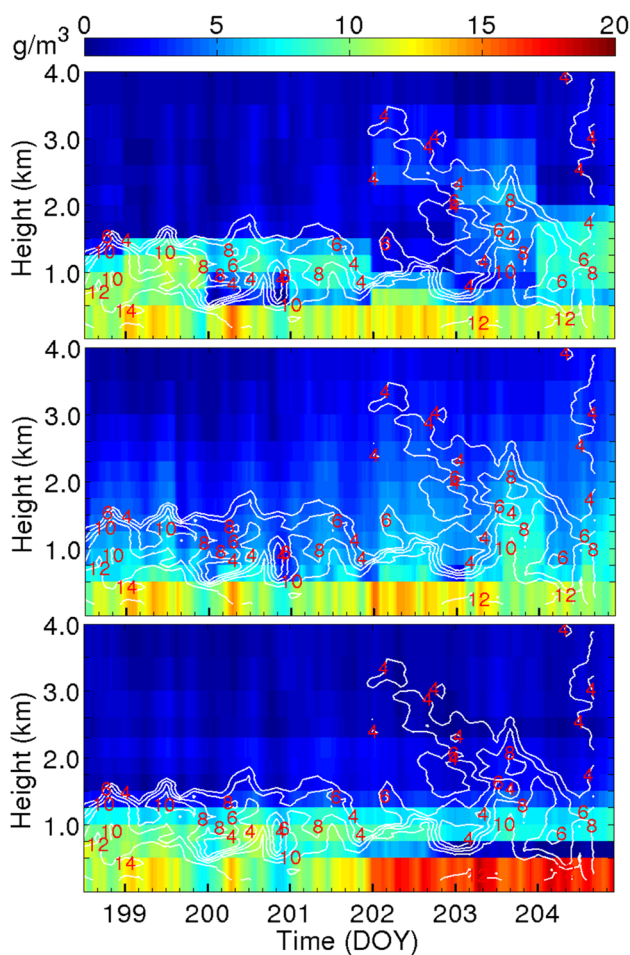

Fig. 5 Evolution of the N_w vertical profile (center grid location) during the entire radiosonde campaign. Tomography solution 1 (radiosonde initialization) (top), tomography solution 2 (AIRS initialization) (center) and tomography solution 3 (radiosonde initialization with no further re-initialization) (bottom). Radiosonde data overlaid in white line contours with red labels

500–1000 m in DOY 199–200, and again on DOY 202–203, when observations indicate water vapor density below 4 g/m^3, is very well reproduced in solution 1 and also present in solution 2. Solution 3 is also able to represent a humidity minimum at the right height, although it tends to drift away from observations, becoming too humid in the bottom 500 m after DOY 202, because it is only updated by GNSS observations after its initialization, The positive anomalies of humidity above 1000 m, namely in DOY 198–199 and 203–204, are also present in solutions 1 and 2.

An objective assessment of the quality of solutions 1 and 3 is presented in Fig. 6, as the RMS error of each solution against the 4-h radiosondes. At 0:00 UTC, solution 1, initialized with radiosonde data, attains a very low RMS which is typically below 0.5 g/m^3, except in DOY 203 where it reaches 1 g/m^3, and then increases during the day until it is comparable with solution 3, as shown by the daily least-squares fitting to solution 1 represented by the dashed blue lines. Regarding solution 3, its quality appears comparable with solution 1 during DOY 199-200-201, showing higher RMS values after that period. In the days after DOY 202, solution 1 drift toward larger RMS values, up to 2.5 g/m^3, possibly due to a change in the synoptic setting, which is characterized by the approach of a weak frontal system near the end of the experiment.

In Fig. 6, DOY 201 stands out as the best in both tomography solutions 1 and 3, and by far the best for solution 3. In this day, solution 3 even outperforms solution 1. Considering that solution 3 is not re-initialized and only evolves due to the GNSS data input, it is interesting to analyze this day in more detail. Figure 7 shows three snapshots of the two solutions, compared with radiosondes at 0:00, 12:00 and 20:00 UTC. At 0:00 UTC, as expected, solution 1 is an almost perfect fit to the radiosonde since it was used for the initialization, while solution 3 fails to see the more humid low-level air near the surface. At this time, the radiosonde
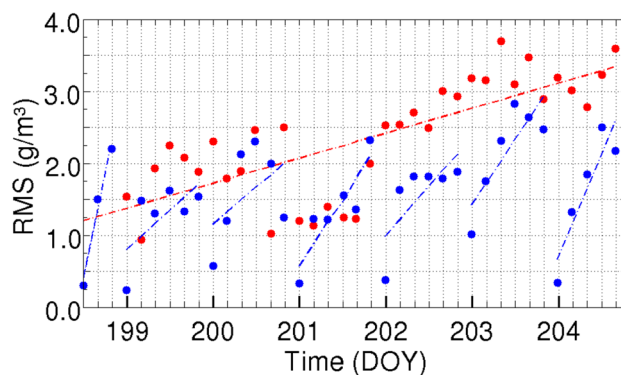

Fig. 6 Evolution of the RMS of solution 1 (blue circles; radiosonde initialization) and solution 3 (red circles; radiosonde initialization with no further re-initialization). Dashed lines represent least-squares fitting: daily in solution 1, all data in solution 3
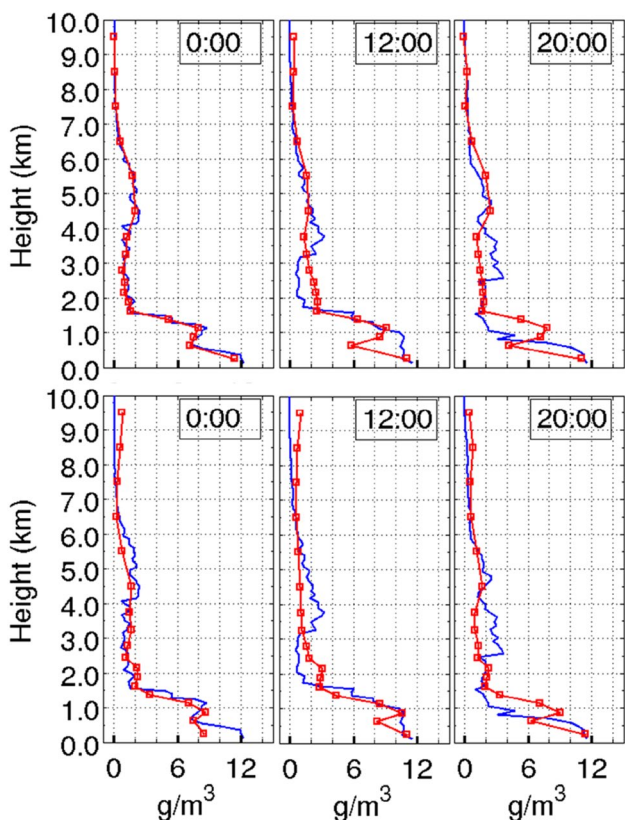
Fig. 7 Comparison of N_w vertical central profile, at DOY 201 and hours 0:00, 12:00, and 20:00 UTC, for tomography solution 1 (radiosonde initialization) (top) and solution 3 (radiosonde initialization with no further re-initialization) (bottom). The blue line corresponds to radiosonde and red line with squares corresponds to tomography

Fig. 8 Boxplot by the hour of RMS differences between radiosonde and the tomography vertical profile solutions: tomography solution 1 (radiosonde initialization) at the top and tomography solution 2 (AIRS initialization) at the bottom

indicates a layer of slightly drier air below 1000 m with below 8 g/m³, topped by a shallow layer slightly wetter with about 9 g/m³, and then a deeper very dry layer (< 2 g/m³) between 2 and 4 km. These features are all present in the two solutions and are very closely matched in solution 1. At 12:00 UTC, the dry layer above 2 km is shallower and tends to subside until 20:00 UTC, constraining the humid boundary layer near the lowest 500 m layer. Solution 1 follows very well the evolution of the lowest layer but tends to produce a dry layer above of that, topped by a more humid layer near 1000 m, which was not observed. Solution 3 also produces a local but more modest spurious minimum near 500 m, and because it also fits observations in the lower layer, leads to a better solution.

The results presented in Figs. 5 and 6 suggest that the frequent assimilation of profile data needed keeps the GNSS tomography solution within reasonable error bounds, as these generally grow in time. Because radiosonde data is expensive and scarce, except during specific localized field experiments, this could suggest that GNSS tomography may be limited to the neighborhood of launching sites. However, Fig. 8 shows
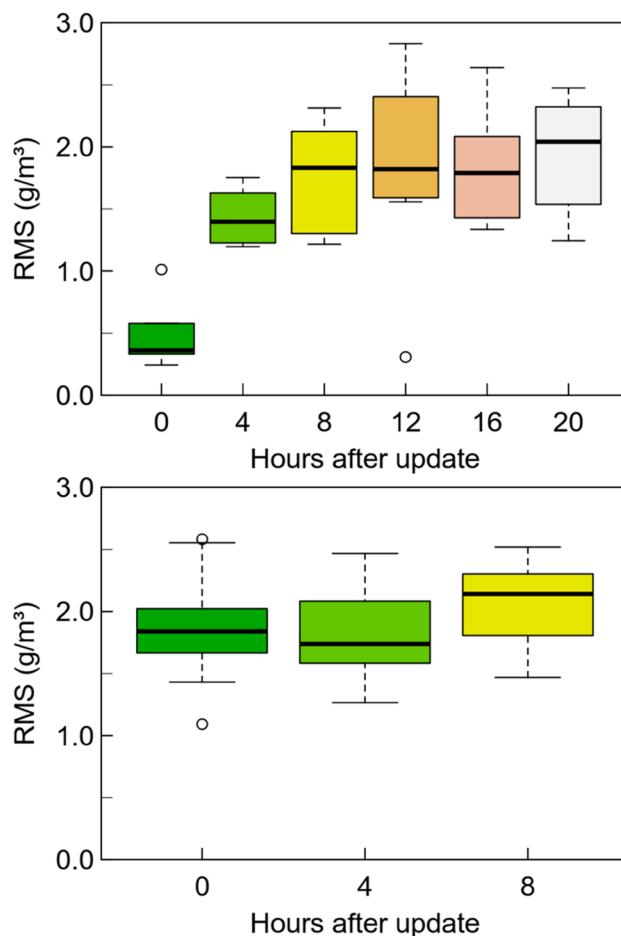
that is not the case. The water vapor RMS values of the tomography solutions 1 and 2 are grouped accounting the time in hours after initialization. The RMS of solution 1 grows gradually until 8 h after the re-initialization when it reaches about 2 g/m³. Except at the radiosonde assimilation time (0:00 UTC), the RMS values of solution 2 are only slightly larger than those of solution 1, taking advantage of the 12-h initialization frequency of the AIRS data compared with the 24-h updating cycle imposed for radiosonde data. Solution 2 also shows narrower error dispersion. Because AIRS is global, it offers data for GNSS assimilation anywhere.

Combining AIRS and radiosonde data into tomography

The general availability of multispectral infrared sounding data and the local availability of at least one daily radiosonde at launching sites suggest that the merging of these two sources could provide a better constraint to GNSS
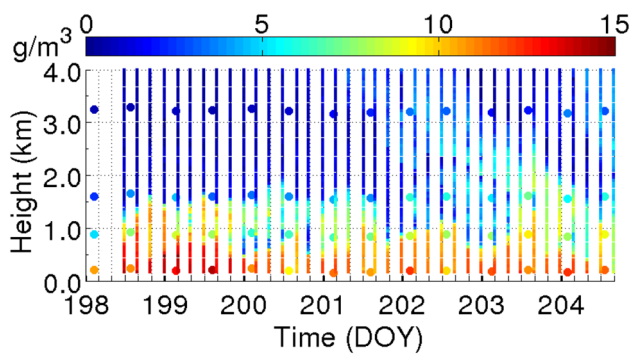
Fig. 9 Vertical profiles of water vapor as estimated by the radiosonde (vertical segments) and AIRS data (circles). Each profile is located at the corresponding acquisition time
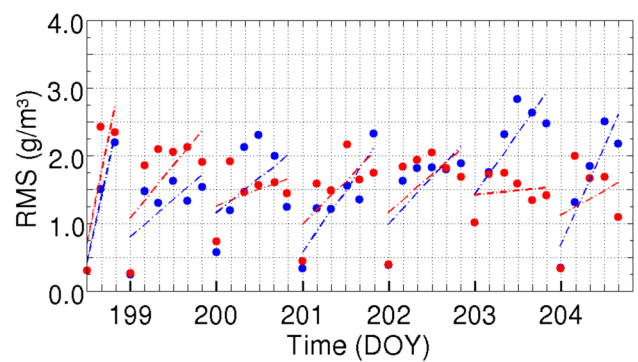

Fig. 10 Evolution of the error of the tomography profile for solutions 1 and 4. Blue circles represent solution 1 (radiosonde initialization) and red circles solution 4 (radiosonde and AIRS initialization). Dashed lines represent daily least-squares fitting for each solution

tomography. As shown in Fig. 9, the AIRS data are at a much lower resolution than radiosondes, and so it is unable to capture localized water vapor anomalies, but it does retrieve the general vertical structure of the water vapor field during the field experiment, as found in other comparisons in different locations (Martins et al. 2010). Figure 8 showed that its impact at assimilation time is rather limited, but it plays a key role in keeping the tomography errors within an error bound comparable with radiosonde initialized solutions, and thus avoiding the long-term error growth observed in solution 3. This result suggested the development of the new solution 4, initialized three times a day from 1 radiosonde (at 0:00 UTC) and the two AIRS profiles.

Figure 10 compares the evolution of the tomography RMS in solution 1 and solution 4. At the radiosonde assimilation time, results are almost identical. At other times, solution 4 is slightly better, especially at the end of the experiment in DOY 203–204, when solution 1 failed to capture the water vapor plume, see Fig. 5, that was better reproduced by solution 2. The increased update frequency of AIRS helps the tomography to better follow a changing atmospheric environment under synoptic forcing. This is similar behavior to what is observed in the assimilation cycle used in the NWM, were usually better results are obtained when more information is introduced into the model.

Conclusion

An experiment has been carried out to evaluate the reliability of GNSS tomography solutions obtained with different data initialization and temporal cycling strategies. Daily radiosondes profiles and AIRS satellite data acquired twice per day were used to initialize tomography solutions. GNSS slant wet delays' tomography observations are computed from 17 GNSS stations deployed over a square area of about 60×60 km^2 in the Lisbon region. These solutions were then evaluated against 4-h radiosonde data acquired during the field experiment. When the initialization of tomography was based on a radiosonde, it was found that the initial solution converged to a profile very close to the one observed, with an error near 0.3 g/m^3, which then increased in time to attain a mean value around 1.5 g/m^3 within a temporal window of about 12 h, not exceeding 3.0 g/m^3 in the following 24 h. When the initialization was made from a much lower resolution AIRS profile, the error presented a much flatter evolution, again never exceeding 3.0 g/m^3, and sometimes smaller than the solution with radiosonde initialization, particularly when the water vapor variability is already well modeled by the GNSS tomography equations. Without any re-initialization, the tomography error increased in time to higher values. The best solution was found by merging one daily radiosonde and the two AIRS soundings in a continuously updated tomography system.

The synoptic conditions observed during the field experiment, typical of a summer day in western Iberia, included significant variations of water vapor in the low troposphere, associated with the sea-breeze circulation (Salgado et al. 2015), and its interaction with Tagus estuary playing the role of a large relatively warm lake. Such circulation produces large horizontal heterogeneities in the water vapor distribution with some signatures in the observed vertical profiles, namely sharp dry intrusions below 1000 m, which are not seen by AIRS and are not possible to assess from GNSS data. In spite of the close spacing of GNSS stations in the experiment, the real horizontal resolution of its water vapor data is rather coarse, as found in Mateus et al. (2018) when compared with much higher resolution InSAR (Interferometry Synthetic Aperture Radar) data.

While the present study was focused in the vertical structure of water vapor fields retrieved from GNSS tomography, which could be objectively evaluated against the frequent radiosondes provided by the field campaign, the method

produces three-dimensional fields of water vapor. The recent study of Mateus et al. (2018), using 3DVAR (three-dimensional variational data assimilation) in a mesoscale forecast model, found that an improvement in that field can have a dramatic impact in the performance of high resolution of weather forecasts of severe weather systems. Considering the critical role of water vapor in most meteorological systems, we expect that similar improvements may be found in non-precipitating systems, such as sea-breeze circulations. The assimilation of tomography retrieved data will be pursued in future work. The possibility of producing improved water vapor atmospheric analysis from the continuous assimilation of GNSS slant delay data, constrained by radiosonde and remote sensed atmospheric profiles in the computation of three-dimensional tomography solutions, offers a new source of valuable data to be assimilated into numerical weather prediction models, at a limited cost, and with the potential of being used by very high-resolution modeling. As suggested by Benevides et al. (2016) that data may be merged with other new generation microwave observations, namely InSAR, also available in all weather conditions and at very high resolution.

References

Aghajany SH, Amerian Y (2017) Three dimensional ray tracing technique for tropospheric water vapor tomography using GPS measurements. J Atmos Solar Terr Phys 164:81–88. https://doi.org/10.1016/j.jastp.2017.08.003

Bender M, Dick G, Ge M, Deng Z, Wickert J, Kahle HG, Raabe A, Tetzlaff G (2011) Development of a GNSS water vapour tomography system using algebraic reconstruction techniques. Adv Space Res 47(10):1704–1720. https://doi.org/10.1016/j.asr.2010.05.034

Benevides P, Catalão J, Miranda PMA (2015a) On the inclusion of GPS precipitable water vapour in the nowcasting of rainfall. Nat Hazards Earth Syst Sci 15(12):2605–2616. https://doi.org/10.5194/nhess-15-2605-2015

Benevides P, Catalao J, Nico G, Miranda PMA (2015b) Inclusion of high resolution MODIS maps on a 3D tropospheric water vapor GPS tomography model. Proc SPIE 9640:96400R. https://doi.org/10.1117/12.2194857

Benevides P, Nico G, Catalão J, Miranda PMA (2016) Bridging InSAR and GPS tomography: a new differential geometrical constraint. IEEE Trans Geosci Remote Sens 54(2):697–702. https://doi.org/10.1109/TGRS.2015.2463263

Benevides P, Nico G, Catalão J, Miranda PMA (2017) Analysis of Galileo and GPS integration for GNSS tomography. IEEE Trans Geosci Remote Sens 55(4):1936–1943. https://doi.org/10.1109/TGRS.2016.2631449

Bevis M, Businger S, Herring T, Rocken C, Anthes R, Ware R (1992) GPS meteorology: remote sensing of atmospheric water vapor using GPS. J Geophys Res 97:15787–15801. https://doi.org/10.1029/92JD01517

Boehm J, Werl B, Schuh H (2006) Troposphere mapping functions for GPS and very long baseline interferometry from European Centre for Medium-Range Weather Forecasts operational analysis data. J Geophys Res Solid Earth. https://doi.org/10.1029/2005JB003629

Brenot H, Walpersdorf A, Reverdy M, Van Baelen J, Ducrocq V, Champollion C, Masson F, Doerflinger E, Collard P, Giroux P (2014) A GPS network for tropospheric tomography in the framework of the Mediterranean hydrometeorological observatory Cévennes-Vivarais (southeastern France). Atmos Meas Tech 7(2):553. https://doi.org/10.5194/amt-7-553-2014

Champollion C (2004) GPS monitoring of the tropospheric water vapor distribution and variation during the 9 September 2002 torrential precipitation episode in the Cévennes (southern France). J Geophys Res 109(D24):D24102

Champollion C, Masson F, Bouin MN, Walpersdorf A, Doerflinger E, Bock O, Van Baelen J (2005) GPS water vapour tomography: preliminary results from the ESCOMPTE field experiment. Atmos Res 74(1):253–274. https://doi.org/10.1016/j.atmosres.2004.04.003

Champollion C, Flamant C, Bock O, Masson F, Turner DD, Weckwerth T (2009) Mesoscale GPS tomography applied to the 12 June 2002 convective initiation event of IHOP_2002. Q J Royal Meteorol Soc 135(640):645–662

Divakarla MG, Barnet CD, Goldberg MD, McMillin LM, Maddy E, Wolf W, Zhou L, Liu X (2006) Validation of Atmospheric Infrared Sounder temperature and water vapor retrievals with matched radiosonde measurements and forecasts. J Geophys Res Atmos. https://doi.org/10.1029/2005JD006116

Flores A, Ruffini G, Rius A (2000) 4D tropospheric tomography using GPS slant wet delays. Ann Geophys 18(2):223–234. https://doi.org/10.1007/s00585-000-0223-7

Guerova G, Jones J, Dousa J, Dick G, de Haan S, Pottiaux E, Bock O, Pacione R, Elgered G, Vedel H, Bender M (2016) Review of the state of the art and future prospects of the ground-based GNSS meteorology in Europe. Atmos Meas Tech 9(11):5385. https://doi.org/10.5194/amt-9-5385-2016

Herring T, King RW, McClusky SC (2010) GAMIT reference manual—GPS analysis at MIT—release 10.4. Department of Earth Atmospheric Planetary Sciences, MIT, Cambridge

Labbouz L, Van Baelen J, Tridon F, Reverdy M, Hagen M, Bender M, Dick G, Gorgas G, Planche C (2013) Precipitation on the lee side of the Vosges Mountains: multi-instrumental study of one case from the COPS campaign. Meteorol Z 22(4):413–432. https://doi.org/10.1127/0941-2948/2013/0413

Lu C, Li X, Ge M, Heinkelmann R, Nilsson T, Soja B, Dick G, Schuh H (2016) Estimation and evaluation of real-time precipitable water vapor from GLONASS and GPS. GPS Solut 20(4):703–713. https://doi.org/10.1007/s10291-015-0479-8

Martins JPA, Teixeira J, Soares PMM, Miranda PMA, Kahn BH, Dang V, Irion B, Fetzer EJ, Fishbein E (2010) Infrared sounding of the trade-wind boundary layer: AIRS and the RICO experiment. Geophys Res Lett 37:L24806. https://doi.org/10.1029/2010GL045902

Mateus P, Nico G, Catalão J (2014) Maps of PWV temporal changes by SAR interferometry: a study on the properties of atmosphere's temperature profiles. IEEE Geosci Remote Sens Lett 11(12):2065–2069

Mateus P, Nico G, Catalão J (2015) Uncertainty assessment of the estimated atmospheric delay obtained by a numerical weather model (NMW). IEEE Trans Geosci Remote Sens 53(12):6710–6717. https://doi.org/10.1109/TGRS.2015.2446758

Mateus P, Miranda PMA, Nico G, Catalão J, Pinto P, Tomé R (2018) Assimilating InSAR maps of water vapor to improve heavy rainfall forecasts: a case study with 2 successive storms. J Geophys

Res Atmos 123(7):3341–3355. https://doi.org/10.1002/2017J D027472

Menke W (2012) Geophysical data analysis: discrete inverse theory. Academic, San Diego

Miranda PMA, Alves JMR, Serra N (2013) Climate change and upwelling: response of Iberian upwelling to atmospheric forcing in a regional climate scenario. Clim Dyn 40(11–12):2813–2824. https://doi.org/10.1007/s00382-012-1442-9

Nilsson T, Gradinarsky L, Elgered G (2007) Water vapour tomography using GPS phase observations: results from the ESCOMPTE experiment. Tellus A 59(5):674–682. https://doi.org/10.111 1/j.1600-0870.2007.00247.x

Olsen ET, Manning E, Blaisdell J, Iredell L, Licata S, Sussking J, Maddy E (2013) AIRS/AMSU/HSB version 6 data release user guide. NASA-JPL Tech Rep, California Institute of Technology Pasadena, Pasadena

Perler D, Geiger A, Hurter F (2011) 4D GPS water vapor tomography: new parameterized approaches. J Geod 85(8):539–550. https://doi.org/10.1007/s00190-011-0454-2

Rohm W (2013) The ground GNSS tomography – unconstrained approach. Adv Space Res 51(3):501–513. https://doi.org/10.1016/j.asr.2012.09.021

Salgado R, Miranda PMA, Lacarrere P, Noilhan J (2015) Boundary layer development and summer circulation in Southern Portugal. Thetys 12:33–44. https://doi.org/10.3369/tethys.2015.12.03

Thayer GD (1974) An improved equation for the radio refractive index of air. Radio Sci 9(10):803–807. https://doi.org/10.1029/RS009 i010p00803

Tregoning P, Herring TA (2006) Impact of a priori zenith hydrostatic delay errors on GPS estimates of station heights and zenith total delays. Geophys Res Lett 33(23). https://doi.org/10.1029/2006G L027706

Zhang K, Manning T, Wu S, Rohm W, Silcock D, Choy S (2015) Capturing the signature of severe weather events in Australia using GPS measurements. IEEE J Sel Topics Appl Earth Obs Remote Sens 8(4):1839–1847. https://doi.org/10.1109/JSTAR S.2015.2406313

Pedro Benevides received his Ph.D. degree in Geographic Engineering from the University of Lisbon in 2016. He is currently working at Instituto Dom Luiz (Lisbon, Portugal). The main research of his work is related to the water vapor studies of the atmosphere through tomography techniques using global navigation satellite system data with auxiliary meteorological and remote sensing datasets.

Joao Catalao received the "licenciatura" degree in 1986 and the Ph.D. degree in 1999, both in Geographic Engineering from the University of Lisbon. He is currently working at Instituto Dom Luiz (Lisbon, Portugal). His research is focused on measuring and monitoring the deformation of the Earth's surface using multiple sensors. At present, his primary interest involves meteorological applications of SAR and GNSS.

Giovanni Nico received the Laurea and Ph.D. degrees in Physics from the University of Bari, Italy, in 1993 and 1999, respectively. He is currently a Researcher with Istituto per le Applicazioni del Calcolo, Consiglio Nazionale delle Ricerche (Bari, Italy). His research interests include space geodesy with emphasis on synthetic aperture radar (SAR) and SAR meteorology, atmospheric physics and big-data in geoinformatics and Earth observation databases.

Pedro M. A. Miranda completed a degree in Physics at the University of Lisbon in 1982, and a Ph.D. degree in Meteorology at the University of Reading, UK, in 1991. He is currently working at the Instituto Dom Luiz and is a Professor of Meteorology at the Faculty of Sciences. His research has been focused on atmospheric and climate modeling, with applications to atmospheric, ocean and climate processes.